

10th Probing the Location and Speciation of Elements in Zeolites with Correlated Atom Probe Tomography and Scanning Transmission X-Ray Microscopy

Joel E. Schmidt,^[a] Xinwei Ye,^[a, b] Ilse K. van Ravenhorst,^[a] Ramon Oord,^[a] David A. Shapiro,^[c] Young-Sang Yu,^[c] Simon R. Bare,^[d] Florian Meirer,^[a] Jonathan D. Poplawsky,^{*[e]} and Bert M. Weckhuysen^{*[a]}

Characterizing materials at nanoscale resolution to provide new insights into structure property performance relationships continues to be a challenging research target due to the inherently low signal from small sample volumes, and is even more difficult for nonconductive materials, such as zeolites. Herein, we present the characterization of a single Cu-exchanged zeolite crystal, namely Cu-SSZ-13, used for NO_x reduction in automotive emissions, that was subject to a simulated 135,000-mile aging. By correlating Atom Probe

Tomography (APT), a single atom microscopy method, and Scanning Transmission X-ray Microscopy (STXM), which produces high spatial resolution X-ray Absorption Near Edge Spectroscopy (XANES) maps, we show that a spatially non-uniform proportion of the Al was removed from the zeolite framework. The techniques reveal that this degradation is heterogeneous at length scales from micrometers to tens of nanometers, providing complementary insight into the long-term deactivation of this catalyst system.

Introduction

Multiscale material complexity and heterogeneity is one of the key drivers for ever more advanced characterization re-

search.^[1-9] Zeolites are heterogeneous catalysts that exhibit such complexity, spanning several orders of magnitude from their catalytic active site (sub-nanometer) to large industrial reactors (tens of meters), and even within single crystals they contain compositional gradients and defects spanning sub-nanometer to micrometer length scales.^[4] There are many characterization techniques that provide spatially resolved information, with varying degrees of chemical information content, but there are few characterization techniques that provide the necessary high spatial resolution and chemical information content. Additionally, many provide only 2D or near-surface information.^[4,5]

Two characterization techniques that provide high spatial resolution information are Atom Probe Tomography (APT) and Scanning Transmission X-ray Microscopy (STXM).^[10-21] APT is a single atom 3-D microscopy that is able to reconstruct the 3-D position and chemical identity of all atoms with sub-nanometer resolution from a needle shaped specimen with dimensions of tens to hundreds of nanometers, making it the highest resolution technique to provide 3-D elemental identification.^[10,11,13-19] STXM relies on a zone plate to focus soft X-rays emitted by a synchrotron onto a small spot on the sample, through which the sample is scanned, and by measuring the total transmitted intensity of the beam as a function of energy it can give information about local chemical environment and abundance. STXM (especially in combination with ptychography) is one of the highest resolution techniques capable of providing this information (possible resolution < 50 × 50 nm² pixel size, and even in the range of 10 nm and below when using ptychography^[22,23]) that is also non-destructive to zeolites as it uses soft X-rays.^[20,21]

- [a] Dr. J. E. Schmidt, X. Ye, I. K. van Ravenhorst, Dr. R. Oord, Dr. F. Meirer, Prof. Dr. B. M. Weckhuysen
Debye Institute for Nanomaterials Science, Faculty of Science
Utrecht University
Utrecht 3584 CG (Netherlands)
E-mail: b.m.weckhuysen@uu.nl
Homepage: <http://www.inorganic-chemistry-and-catalysis.eu/home.html>
- [b] X. Ye
School of Materials Science and Engineering
Key Laboratory of Advanced Energy Materials Chemistry (MOE)
Collaborative Innovation Center of Chemical Science and Engineering
Nankai University
Tianjin 300350 (P.R. China)
- [c] Dr. D. A. Shapiro, Dr. Y.-S. Yu
Advanced Light Source
Lawrence Berkeley National Laboratory
Berkeley CA, 94720 (USA)
- [d] Dr. S. R. Bare
SLAC National Accelerator Laboratory
Menlo Park CA 94025 (USA)
- [e] Dr. J. D. Poplawsky
Center for Nanophase Materials Sciences
Oak Ridge National Laboratory
Oak Ridge, TN 37831 (USA)
E-mail: poplawskyjd@ornl.gov

Supporting information for this article is available on the WWW under <https://doi.org/10.1002/cctc.201801378>

This manuscript is part of the Anniversary Issue in celebration of 10 years of ChemCatChem.

© 2019 The Authors. Published by Wiley-VCH Verlag GmbH & Co. KGaA. This is an open access article under the terms of the Creative Commons Attribution Non-Commercial NoDerivs License, which permits use and distribution in any medium, provided the original work is properly cited, the use is non-commercial and no modifications or adaptations are made.

Both APT and STXM have been applied to zeolite-based catalysts by a number of research groups, resulting in a significant body of accumulated knowledge.^[20,24–34] However, to the best of our knowledge, there are no reports that correlate results of the two characterization techniques. Herein, we have applied APT and STXM in an integrated fashion to study the same single crystal of a laboratory aged (135,000 mile simulation) sample of copper-exchanged zeolite SSZ-13 (Cu-SSZ-13, CHA framework topology), which is the same sample as we previously studied with APT alone.^[29] We chose this sample as the $\sim 4\ \mu\text{m}$ crystal size makes spatially resolved characterization studies meaningful, and as the sample was previously studied any potential beam damage can be assessed, a known problem when probing zeolites with electron beams.^[35] Further, the ion exchange with Cu-ions makes this a difficult material to characterize with conventional ^{27}Al Magic Angle Spinning solid-state Nuclear Magnetic Resonance (MAS ssNMR) spectroscopy due to interference from paramagnetic Cu, motivating us to explore other characterization methods. Our results indicate that it is possible to correlate the results of these two high-resolution techniques, and thereby gain information on the location and local environment of the elements present to construct a more complete understanding of how the material resists deactivation under demanding tailpipe conditions.

Results and Discussion

The STXM experiments were performed at the Advanced Light Source (ALS, Berkeley, California, USA) beamline 11.02 and the sample preparation and APT experiments were conducted at the Center for Nanophase Materials Sciences (CNMS) at Oak Ridge National Laboratory (ORNL, Oak Ridge, Tennessee, USA). Prior to the STXM experiment, a single crystal of aged zeolite Cu-SSZ-13 was attached to a Mo Omniprobe® Lift-Out Grid (Mo was used to prevent any contamination from a more typical Cu grid), and thinned to $\sim 0.5\ \mu\text{m}$ using Focused Ion Beam (FIB) milling to allow for sufficient X-ray transmission through the material, as is shown in Figure 1c to f.^[36] The aged zeolite Cu-SSZ-13 is the same as reported in reference [29], with a bulk Si/Al ratio of ~ 20 , and was aged using the industry standard simulation for a 135,000 mile vehicle-aged catalyst.^[37] After being mounted on the grid and thinned, the zeolite crystal had an asymmetrical Pt coating deposited on the crystal surface (Figure 1e, FIB Pt was deposited on the crystal surface to protect the material during milling), which served as a marker for the correlated experiments. Careful examination of Figure 1f shows that the crystal thickness is not uniform and it is thinner at the top near the Pt strip, this was a consequence of the FIB milling step with the Ga ion source normal to the top of the

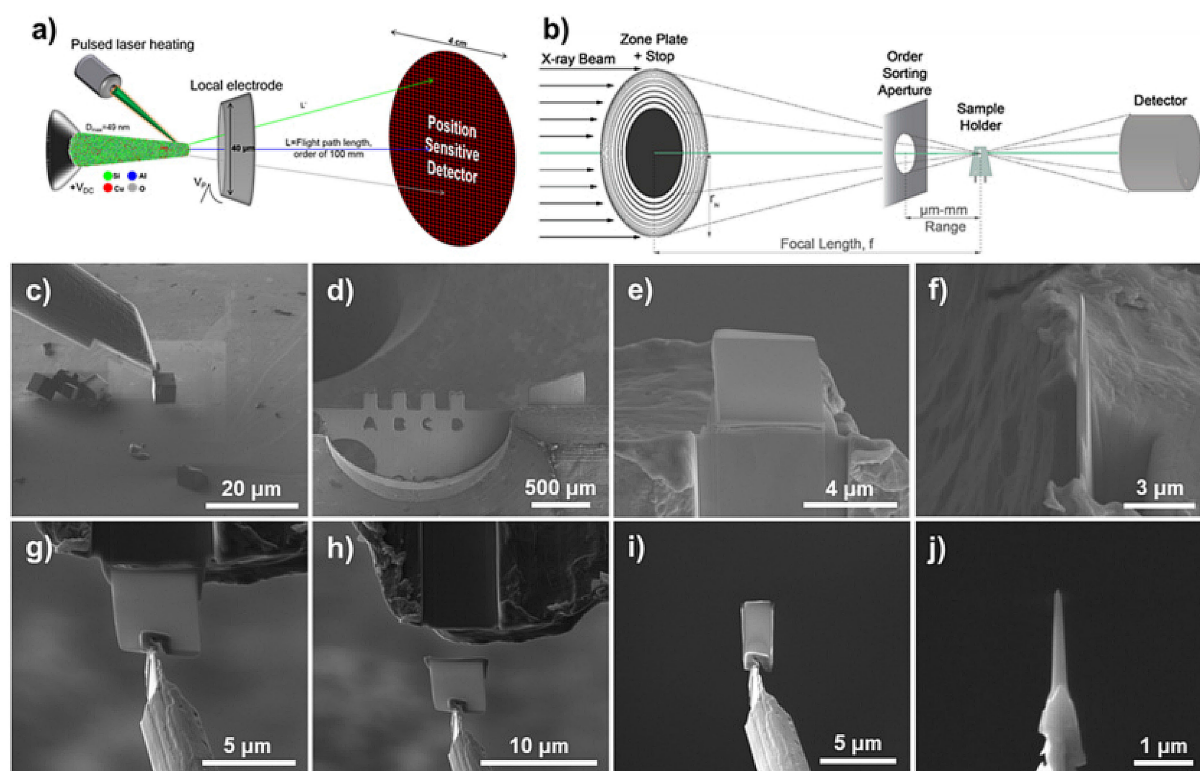


Figure 1. Overviews of characterization techniques and sample preparation for Atom Probe Tomography (APT) and Scanning Transmission X-ray Microscopy (STXM). (a) Schematic of an APT instrument, including approximate sizes of the various components. (b) Schematic of a STXM instrument with important components: Soft X-ray beam, zone plate, Order Sorting Aperture (OSA), sample holder and detector. (c–f) Picking up a single crystal of zeolite Cu-SSZ-13 using a Kleindiek nanomanipulator and then attaching the crystal to a Mo Omniprobe® Lift-Out Grid using Focused Ion Beam (FIB) Pt and subsequently thinning the crystal to $\sim 0.5\ \mu\text{m}$ using a Ga FIB milling after applying a protective Pt layer shown in e. (g–j) After the STXM measurements the cross section is attached to the tungsten needle on the Kleindiek nanomanipulator where it is shaped into a needle for the APT experiment which was performed on the tungsten needle instead of the typical Si micro-tip array.

crystal, and the top was thinner as it was more exposed to the Ga ion beam. After the zeolite crystal was mounted at CNMS it was transferred to ALS for the STXM experiment.

The cross section was loaded into the STXM instrument and a transmission image was first recorded at the Al pre-edge energy of 1561.0 eV and is compared to the SEM image in Figure 2a and b. The STXM measurement was conducted with the soft X-ray beam going through a 45 nm zone plate (ZP), resulting in a $50 \times 50 \text{ nm}^2$ beam spot size. The Pt deposited to protect the sample during FIB milling is evident in the transmission image due to its stronger absorption caused by its high density, and the non-symmetrical Pt deposition then acts as a marker for the crystal edge. The bulk XANES from combining all data collected for the cross section is shown in Figure 2h along with the references for tetrahedral and octahedral Al, which were zeolite ZSM-5 and $\alpha\text{-Al}_2\text{O}_3$, respectively. The linear combination fitting (Figure 2h and Table 1) shows that the cross section contains $\sim 90\%$ tetrahedral Al (framework) and $\sim 10\%$ octahedral Al (extra-framework). This relatively small proportion of framework Al removal to form octahedral Al is consistent with the results of previous studies, and is expected from our previous study of this material and is also consistent with the catalyst retaining its activity after aging.^[29,38–40]

Table 1. Linear combination fitting of Al K-edge XANES of the bulk and clusters employing ZSM-5 and $\alpha\text{-Al}_2\text{O}_3$ as references for tetrahedral Al (Al_{Td} framework) and octahedral Al (Al_{Oh} , extra-framework) respectively.

	Al_{Oh}	+/-	Al_{Td}	+/-	R-square	R-factor	Reduced chi-square
Bulk XANES	0.092	0.108	0.908	0.136	0.786	0.036	0.079
Cluster 1	0.159	0.225	0.841	0.284	3.408	0.102	0.341
Cluster 2	0.065	0.110	0.935	0.138	0.812	0.037	0.081
Cluster 3	0.000	0.160	1.000	0.202	1.727	0.147	0.173

In the transmission image at 1561.0 eV in Figure 2b a pixel size of $50 \times 50 \text{ nm}^2$ was used. For further analysis the transmission image was first converted to display absorption, i.e. the X-ray absorption coefficient. Then, the 52 images of the X-ray energy scans were spatially aligned followed by removal of the region which did not contain zeolite resulting in a $3.4 \times 2.4 \mu\text{m}^2$ scan area. Once the XANES of each pixel were examined it was evident that the absorption was not sufficient to give enough signal for the single pixel X-ray absorption spectra to be meaningfully analyzed. Therefore, the images were binned to combine 4 (2×2) pixels into one. Then there were 34×24 pixels

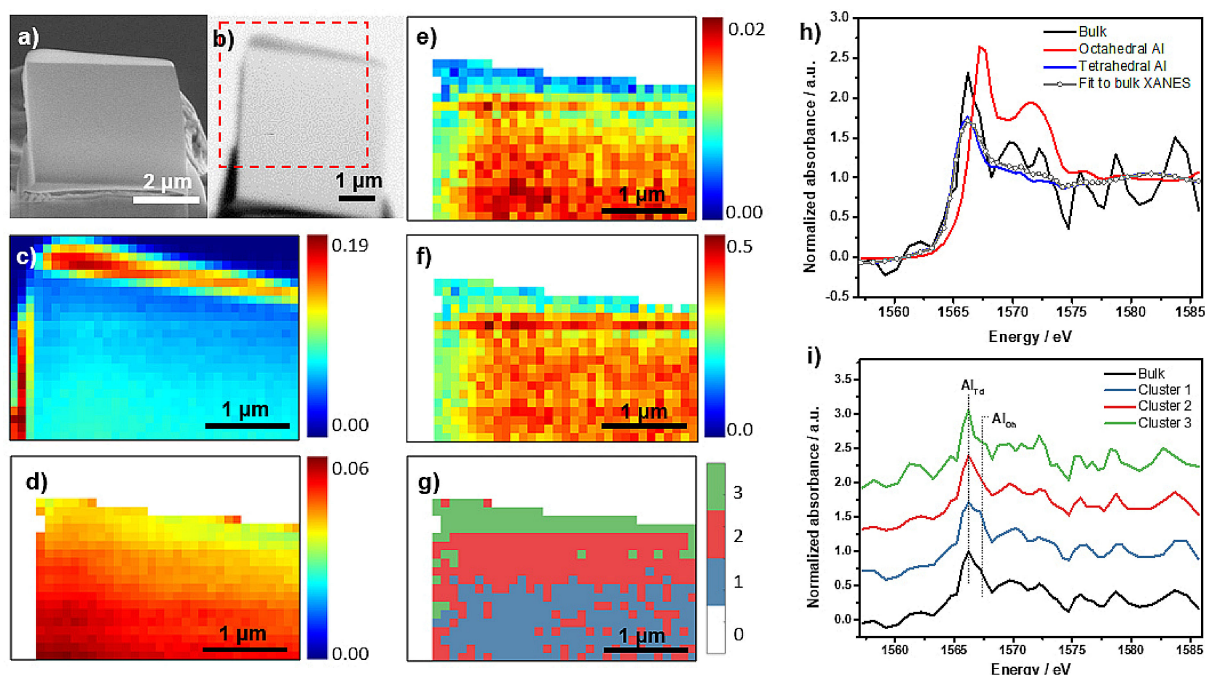


Figure 2. (a) Scanning electron microscope (SEM) image of the cross section mounted for the Scanning Transmission X-ray Microscopy (STXM) experiment. (b) Transmission image of the entire cross section recorded at 1561.0 eV. The red rectangle indicates the scanning area in STXM, which was collected with a field of view (FOV) of $4 \times 4 \mu\text{m}^2$ or 80×80 pixels (pixel size: $50 \times 50 \text{ nm}^2$). Area shown in figure c-g is part of the scanning region that was designated for STXM-XANES analysis with a FOV of $3.4 \times 2.4 \mu\text{m}^2$ or 34×24 pixels (pixel size $100 \times 100 \text{ nm}^2$, binning 0.5). (c) STXM optical density of the cross section at 1566.2 eV, which was converted from the as-recorded transmission image, showing the maximum absorption contrast. The scale bar indicates the X-ray absorption intensity. (d) Average STXM optical density of the cross section in pre-edge region after applying a mask to remove all data except the crystal, showing the thickness difference within the crystal. The scale bar indicates the absorption intensity of X-rays. (e) Edge-jump map based on XANES representing Al amount. The scale bar reports the values of the absorption edge jump, defined as the difference between the average intensity value in the XANES post-edge region and the average intensity value in the XANES pre-edge region. (f) Thickness-corrected edge jump map based on XANES representing Al concentration. The scale bar indicates the absorption intensity of X-ray. (g) The result of segmentation based on PCA and clustering analysis of the cross section showing the spatial distribution of the three clusters, with XANES for each cluster in (i). (h) Linear combination fitting of XANES of the bulk employing zeolite ZSM-5 and $\alpha\text{-Al}_2\text{O}_3$ as reference for tetrahedral Al and octahedral Al, respectively. (i) Bulk XANES for the entire cross section along with the XANES for the three clusters isolated by PCA and clustering analysis.

remaining, and after filtering out the region that did not contain zeolite or had Pt deposition using a mask (details in experimental section), 538 pixels remained for analysis. After binning and applying the data mask, the absorption map based on the average absorption in the pre-edge region (1557–1563 eV) is shown in Figure 2d. This figure shows that the absorption increases from the top to the bottom of the sample as expected due to the increasing sample thickness; the X-ray absorption in the pre-edge region is a good measure for sample thickness as it is not (or only very little) influenced by relative changes in Al concentration.

The amount of Al within the cross section was evaluated by studying the absorption edge jump map, shown in Figure 2e. The data in the figure are consistent with a gradient in Al with the lowest amount near the top of the crystal. At first consideration, this would appear to indicate Al zoning across the cross section. However, closer examination of the side view of the cross section by SEM (Figure 1f) shows that the FIB milling used to thin the zeolite crystal left the cross section thinner at the top than the bottom, which is a common occurrence as the milling ion beam source was normal to the top of the crystal. To exclude the absorption difference due to varying thickness, the edge jump map is divided by the average pre-edge absorption in each pixel to obtain the thickness-corrected edge jump map (Figure 2f), which then shows the Al concentration in each pixel. This figure shows that there is a higher thickness-corrected absorption in the center of crystal compared to both edges, which would mean the Al concentration is lower near the crystal edge (~100–300 nm) than the rest of the crystal. However, we want to further explore this result due to any possible influence of the protective Pt layer applied to the material. Though, it is certainly shown that the Al concentration is homogeneous within the central region of the crystal at the scale of $100 \times 100 \text{ nm}^2$ pixels that were analyzed, though not in the first ~100–300 nm near the crystal surface.

As the single pixel XANES is too noisy to provide useful edge energy information, which could be used to distinguish tetrahedral versus octahedral Al, the data was further analyzed using Principal Component Analysis (PCA). The influence of sample thickness was excluded in the PCA by using normalized data (edge jump set to one). Furthermore, PCA is conducted without any *a priori* knowledge of the data, so it is an unbiased method of analysis. PCA of the XANES maps indicated two main components, and further clustering analysis demonstrated three significantly different clusters in the cross section, as shown in Figure 2i, with the deconvolutions and resulting amounts of tetrahedral and octahedral Al in each cluster given in Figure 3 and Table 1. The fitting procedure is described in the experimental section, and is very sensitive to the absorption edge shift, so the differences between the curves are subtle, but significant, as the use of PCA and clustering analysis was necessary to extract three different clusters from the data. The three clusters have an increasing amount of octahedral Al, from none in cluster 3, which is near the edge of the crystal, to ~15% octahedral Al near the center. Based on the PCA and clustering analysis of the Al map it appears that steaming causes a more significant fraction of framework Al to be

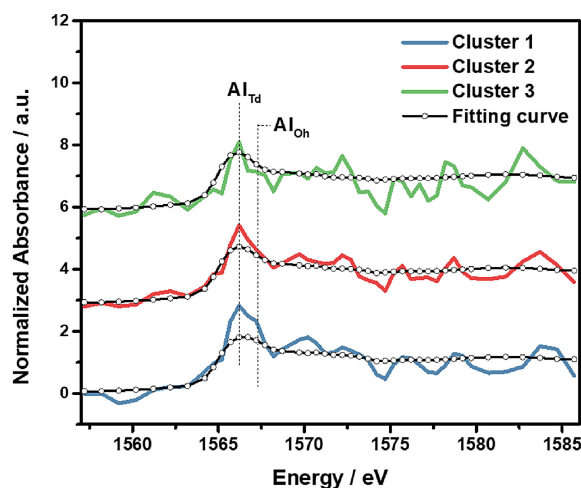


Figure 3. Linear combination fitting of XANES of the three clusters identified using PCA and clustering analysis, and employing zeolite ZSM-5 and $\alpha\text{-Al}_2\text{O}_3$ as references for tetrahedral Al and octahedral Al, respectively. The results are given in Table 1. Note that the shoulder for octahedral Al in cluster 1 is especially prominent relative to clusters 2 and 3.

removed near the center of the crystal compared to the edge of the crystal. As the thickness corrected edge jump map showed a lower Al concentration near the edge it may mean that in the Al rich central region the Al was more easily removed from the framework. This nanoscale identification of an increasing amount of framework Al removal with increasing Al concentration is consistent with the general macroscale trend in zeolite catalysts, that materials are less stable to hydrothermal treatment when they have a higher amount of Al, that is, a lower Si/Al ratio.^[41]

After the successful STXM data collection the lift-out was returned to ORNL's CNMS for the APT experiment. As shown in Figure 1, a single needle could be extracted from the cross section, and instead of being attached to a standard, commercially produced Si microtip array, the APT experiment was performed on a tungsten wire that had been sharpened by electropolishing. This is the more traditional method of running APT experiments, and while it is more labor-intensive than using a Si microtip array, the small size of the cross section would have made it difficult to use a microtip array.^[42–44] The APT experiment was successful, and 1.3 million ions were collected. This is a sufficient data set for analysis. Views of all Al and Cu atoms are shown in Figure 4a and Movie S1, and, as expected from our previous study, the Al distribution appears to be visually heterogeneous.^[29] The distributions of Cu and Al were analyzed using the Nearest Neighbor Distributions (NNDs) and Radial Distribution Functions (RDFs), shown in Figure 4. For the NNDs, the 4th NND is shown as it led to a better separation between the collected and randomized data, and for Cu there is clearly a non-random distribution, while for Al there appears to be a small difference between the collected and randomized data. The Al RDF (Figure 4c) indicates an Al–Al and Al–Cu affinity, consistent with previous findings. Interestingly, in the Cu RDF there is a clear Cu–Cu affinity, but no Cu–Al affinity, and this result contrasts with the two needles we previously studied

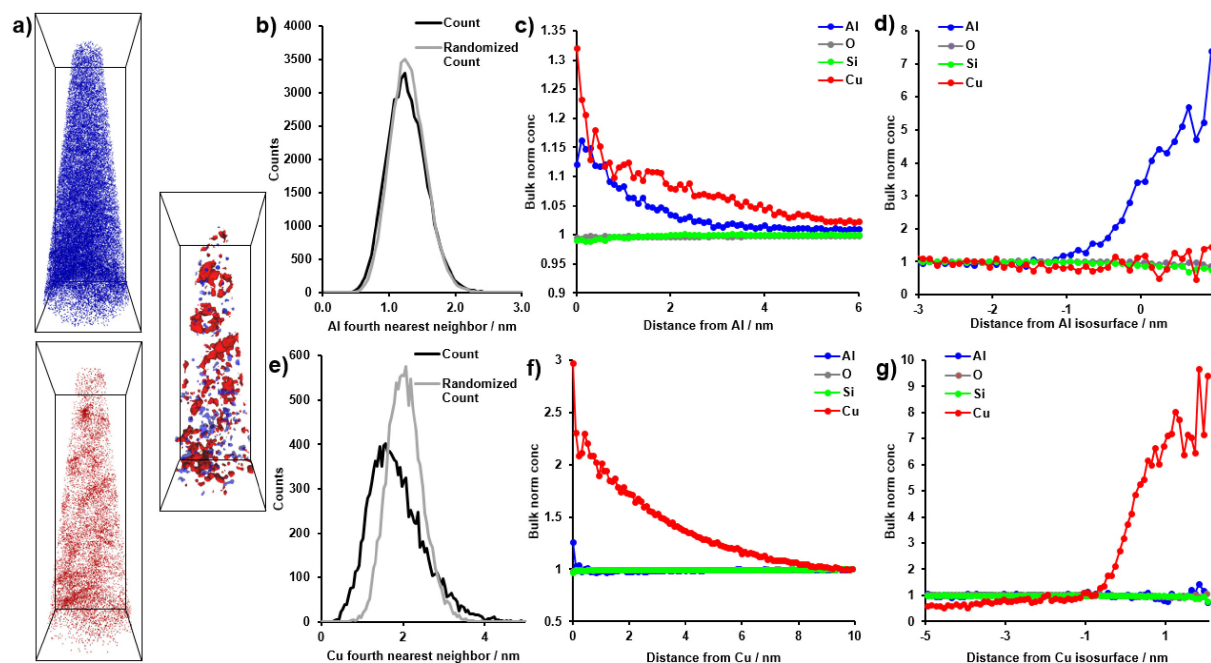


Figure 4. Results of the Atom Probe Tomography (APT) experiments and data analysis. (a) Distributions of all Al ions (blue) and all Cu ions (red) as well as 5.6% Al isosurfaces (blue) and 2% Cu isosurfaces (red), bounding box dimensions $143 \times 48 \times 49 \text{ nm}^3$. (b) Al fourth nearest neighbor distribution (4NND). (c) Al radial distribution function (RDF). (d) Proximity histogram across the 5.6% Al isoconcentration surface shown in (a), with bulk normalized concentrations shown. (e) Cu 4NND. (f) Cu RDF. (g) Proximity histogram across the 2% Cu isoconcentration surface shown in (a), with bulk normalized concentrations shown.

from this sample. The heterogeneous distributions of both Al and Cu were then analyzed using isosurface analysis, and 2% Cu and 5.6% Al isoconcentration surfaces are shown in Figure 4 along with proximity histograms. The proximity histograms indicate Cu–Cu and Al–Al affinity, but not a significant affinity of Cu–Al or Al–Cu. This is similar to what we previously found and is in line with the robust stability of zeolite Cu-SSZ-13, as we have not been able to identify any regions with a composition similar to copper aluminate spinel (*i.e.*, CuAl_2O_4), which could be quantitatively identified in aged zeolite Cu-ZSM-5.^[29] Overall, the APT analysis of this needle gave results consistent with our previous study, except for not finding a significant Cu–Al affinity in the RDF. We do not know if this is due to damage to the material or variations in the material, though we believe the latter is more likely as beam damage generally causes aggregation of chemical elements, which is opposite to our findings here.

To attempt to correlate results of the two nanoscale chemical imaging techniques, Figure 1h–j shows that the needle was removed from nearer the center of the region measured by STXM as shown in Figure 2a and b. This is the portion of the needle that contained $\sim 15\%$ octahedral Al from the XANES cluster analysis. The APT analysis found heterogeneities in the Al distribution, which would be consistent with damage from the material due to steaming. This has been established in studies of pristine and steamed zeolite ZSM-5 crystals, where heterogeneities in the Al distribution were only found by APT after steaming.^[24] In the present study the Al distribution is only slightly heterogeneous, consistent with the preserved catalytic

activity after the simulated aging, and the relatively small fraction of octahedral Al identified using STXM.

This study has provided new information regarding the deactivation of Cu-SSZ-13 under tailpipe conditions. Of special importance is the zoning identified in the removal of framework (tetrahedral) Al to form extraframework (octahedral) Al. These species are not desirable as they can lead to the nonselective oxidation of ammonia, such that the NO_x is not efficiently reduced. Finding that framework Al is preferentially removed near the center of the zeolite crystal shows that it may be important to better engineer zeolite catalysts to avoid this. It also shows that bulk studies may underestimate the severity of material damage as we found that the majority of the degradation occurred near the center, which means NH_3 -SCR reactants may never see the damaged region as they must diffuse through the undamaged region first, where the NO_x reduction reaction can occur, allowing even damaged crystals to show high activity.

Correlating APT and STXM experiments has been demonstrated to be possible, though it should be clear that it remains technically challenging. Some of the unique advantages of using this correlated characterization approach are: i) APT can resolve the 3-D location of all elements, but gives no information about their local bonding environment which can be gained from STXM. ii) Since STXM uses soft X-rays it has been estimated that radiation damage effects are two orders of magnitude lower than for Electron Energy Loss Spectroscopy (EELS) measured in a TEM, another technique capable of giving high spatial resolution spectral information.^[20,45,46] As we previously studied this sample we could compare the results,

and did not find evidence of significant damage from the STXM experiment. Some of the disadvantages to this correlated approach are: i) The (current) spot size of STXM used (i.e., 50 nm) is similar to the diameter of the needle measured for APT, making it difficult to find any STXM spatial resolution within an APT needle, though the heterogeneities found using cluster analysis were larger regions, making some correlation possible. ii) Specific to our experiment, zeolite samples need to be $>0.5\ \mu\text{m}$ thick for sufficient X-ray absorption, but this is much larger than the dimensions of a typical APT needle, making spatial correlations difficult because the STXM information gives 2-D maps, so it can be difficult to correlate the two characterization techniques. Therefore, it may be more practical to study a material with a smaller absorption length which may enable a more meaningful, spatially resolved correlation to be made between the two techniques. This would likely be a dense metal, and it may allow for further advances in correlating these techniques and further technical developments. In any case, we have clearly demonstrated that correlative STXM-APT is feasible, opening new directions in nanoscale chemical imaging of solid catalysts.

Experimental Section

The aged zeolite Cu-SSZ-13 is the same as reported in reference [29], with a bulk Si/Al ratio of ~ 20 , and was aged using the industry standard simulation for a 135,000 mile vehicle-aged catalyst, as described in our recent manuscript. Crystals of aged zeolite Cu-SSZ-13 were attached to Omniprobe[®] Lift-Out Grids and thinned to $0.5\ \mu\text{m}$, as shown in Figure 1, using a Ga Focused Ion Beam (FIB) and Kleindiek nanomanipulator.^[29] For the STXM experiment the grid was attached to the sample holder using double sided tape. The sample chamber was evacuated and then backfilled with He to a pressure of 200 Torr. The STXM measurements on the cross section were performed at the Advanced Light Source (ALS) beamline 11.0.2 of Lawrence Berkeley National Laboratory, Berkeley, California, USA.^[47,48] The soft X-ray beam focused on the sample with a 50 nm spot size after going through a 45 nm Zone Plate (ZP) and sequentially an Order Sorting Aperture (OSA) with a $90\ \mu\text{m}$ pinhole. The focused X-ray beam reached the sample to form a point-by-point image by moving the sample plate step by step, resulting in an X-ray absorption spectrum at each pixel. A stack of transmission images with a $4 \times 4\ \mu\text{m}^2$ Field of View (FOV) and $50 \times 50\ \text{nm}^2$ pixel size, was obtained by varying the incident X-ray energy in the energy region of 1557–1585 eV for Al K-edge imaging. Because the Cu concentration was too low to detect we did not perform STXM on Cu L-edge of the cross section.

STXM-XANES data of the cross section was analyzed using the aXis2000 (<http://unicorn.mcmaster.ca/aXis2000.html>) and TXM-Wizard^[49] software packages. A stack of transmission images, recorded in energy sequences, was aligned in aXis2000 to ensure the cross section position remained stable. The aligned transmission images were then converted to absorbance mode represented as Optical Density (OD), by defining the Absorbance (A) as $A = -\ln(I/I_0)$, where I_0 and I are X-ray intensities before and after going through the sample.^[21] The stack of OD images was subsequently loaded in the TXM-Wizard software to obtain detailed analysis on chemical composition and spatial distribution of Al. The stack of images was cropped and binned by combining 2×2 pixels² into one to enhance the signal to noise ratio in XANES through lowering spatial resolution, resulting in images with a $3.4 \times 2.4\ \mu\text{m}^2$ FOV and $100 \times$

$100\ \text{nm}^2$ pixel size. To analyze the area without any interfering absorption from deposited Pt, a mask was created using Principal Component Analysis (PCA) of the raw data, which clearly separated the zeolite from background and Pt. Subsequently, the mask was used to filter the background area and deposited Pt in the cross section. Therefore, only pixels showing an edge jump at the Al K-edge were left to conduct further analysis.

The bulk spectrum was obtained after employing this mask and the edge jump filter, which was employed to filter pixels with extremely low energy jump, i.e. pixels dominated by noise. The bulk XANES was taken as the average spectrum of all remaining single pixel spectra in the image. Energy calibration of the Al K-edge XANES was carried out by shifting the white line maximum of the bulk spectrum to 1566.2 eV, referring to the Al K-edge XANES of ZSM-5 used as a standard and measured previously by our group.^[25] The local chemical environment of Al in the cross section was analyzed by Least Square Linear Combination (LSLC) fitting of the bulk XANES, taking zeolite ZSM-5 and $\alpha\text{-Al}_2\text{O}_3$ as references for tetrahedral Al and octahedral Al, respectively. The fitting range covered the edge region from 1563.20 eV to 1568.70 eV.

An edge jump filter was employed to remove the noisy pixels based on the noise level of the pre-edge region and the difference between the pre-edge and the post-edge, followed by applying a normalization filter and removing pixels with distorted a pre-edge or post-edge. PCA and k -means clustering were then performed to pool pixels into different clusters based on the similarity of their XANES. According to the eigenspectra and the scree plot, the first two Principal Components (PCs), which could explain more than 95% of data variance, were chosen. Next, the data was projected onto this 2-dimensional PC space and upon inspection of the resulting score plot classified into three clusters ($k=3$) via k -means clustering using the average solution of 10 k -means replicates. Using this result as an initial solution the clustering was further refined by an Expectation Maximization (EM) algorithm for Gaussian Mixture Modeling (GMM) to achieve a point density clustering in PC space, which often improves the clustering for noisy XANES data. Species of Al were determined by LSLC fitting of the XANES of the clusters using the same procedure as for the bulk XANES.

After STXM measurements, a needle shaped specimen was carefully removed from the cross section using Ga FIB milling and then studied with APT using the LEAP 4000XR local electrode atom probe equipped with laser pulsing capabilities and an energy compensating reflectron lens and data analysis was performed using CAMECA's IVAS software. We have previously reported both in detail.^[13,28,29,50] The APT experiment was performed on a tungsten wire instead of a Si micropost array, which is the more historical method of conducting APT experiments.^[42–44]

Acknowledgements

This work is supported by the NWO Gravitation program, Netherlands Center for Multiscale Catalytic Energy Conversion (MCEC), and a European Research Council (ERC) Advanced Grant (No. 321140). The APT measurements were conducted at the Center for Nanophase Materials Sciences, which is a DOE Office of Science User Facility. J.S. has received funding under the Marie Skłodowska-Curie Grant Agreement No. 702149. X.Y. acknowledges support from China Scholarship Council (CSC). This research used resources of the Advanced Light Source, which is a U.S. DOE Office of Science User Facility under contract no. DE-AC02-05CH11231. This manuscript has been authored by UT-Battelle, LLC under

contract number DE-AC05-00OR22725 with the U.S. Department of Energy. The United States Government retains and the publisher, by accepting the article for publication, acknowledges that the United States Government retains a non-exclusive, paid-up, irrevocable, world-wide license to publish or reproduce the published form of this manuscript, or allow others to do so, for United States Government purposes. The Department of Energy will provide public access to these results of federally sponsored research in accordance with the DOE Public Access Plan (<http://energy.gov/downloads/doe-public-access-plan>).

Conflict of Interest

The authors declare no conflict of interest.

Keywords: scanning transmission X-ray microscopy · atom probe tomography · zeolites · NO_x reduction · chemical imaging

- [1] K. Morgan, J. Touitou, J.-S. Choi, C. Coney, C. Hardacre, J. A. Pihl, C. E. Stere, M.-Y. Kim, C. Stewart, A. Goguet, W. P. Partridge, *ACS Catal.* **2016**, *6*, 1356–1381.
- [2] A. Urakawa, A. Baiker, *Top. Catal.* **2009**, *52*, 1312–1322.
- [3] B. M. Weckhuysen, *Angew. Chem. Int. Ed.* **2009**, *48*, 4910–4943; *Angew. Chem.* **2009**, *121*, 5008–5043.
- [4] I. L. C. Buurmans, B. M. Weckhuysen, *Nat. Chem.* **2012**, *4*, 873–886.
- [5] G. Möbus, B. J. Inkson, *Mater. Today* **2007**, *10*, 18–25.
- [6] E. Mahmoud, R. F. Lobo, *Microporous Mesoporous Mater.* **2014**, *189*, 97–106.
- [7] Z. Liu, N. Fujita, K. Miyasaka, L. Han, S. M. Stevens, M. Suga, S. Asahina, B. Slater, C. Xiao, Y. Sakamoto, M. W. Anderson, R. Ryoo, O. Terasaki, *Microscopy* **2013**, *62*, 109–146.
- [8] C. Chmelik, J. Kärger, *Chem. Soc. Rev.* **2010**, *39*, 4864–4884.
- [9] K. P. F. Janssen, G. De Cremer, R. K. Neely, A. V. Kubarev, J. Van Loon, J. A. Martens, D. E. De Vos, M. B. J. Roeffaers, J. Hofkens, *Chem. Soc. Rev.* **2014**, *43*, 990–1006.
- [10] A. Devaraj, D. E. Perea, J. Liu, L. M. Gordon, T. J. Prosa, P. Parikh, D. R. Diercks, S. Meher, R. P. Kolli, Y. S. Meng, S. Thevuthasan, *Int. Mater. Rev.* **2018**, *63*, 68–101.
- [11] Y. Amouyal, G. Schmitz, *MRS Bull.* **2016**, *41*, 13–18.
- [12] F. Meirer, B. M. Weckhuysen, *Nat. Rev. Mater.* **2018**, *3*, 324–340.
- [13] J. E. Schmidt, L. Peng, J. D. Poplawsky, B. M. Weckhuysen, *Angew. Chem. Int. Ed.* **2018**, *57*, 10422–10435; *Angew. Chem.* **2018**, *130*, 10580–10593.
- [14] M. K. Miller, R. G. Forbes, *Atom-Probe Tomography*, Springer, Boston, **2014**.
- [15] M. K. Miller, T. F. Kelly, K. Rajan, S. P. Ringer, *Mater. Today* **2012**, *15*, 158–165.
- [16] T. F. Kelly, D. J. Larson, *MRS Bull.* **2012**, *37*, 150–158.
- [17] M. K. Miller, R. G. Forbes, *Mater. Charact.* **2009**, *60*, 461–469.
- [18] T. F. Kelly, M. K. Miller, *Rev. Sci. Instrum.* **2007**, *78*, 031101.
- [19] M. K. Miller, *Atom Probe Tomography*, Springer, Boston, **2000**.
- [20] F. M. F. de Groot, E. de Smit, M. M. van Schooneveld, L. R. Aramburo, B. M. Weckhuysen, *ChemPhysChem* **2010**, *11*, 951–962.
- [21] E. de Smit, I. Swart, J. F. Creemer, G. H. Hovelting, M. K. Gilles, T. Tyliczszak, P. J. Kooyman, H. W. Zandbergen, C. Morin, B. M. Weckhuysen, F. M. F. de Groot, *Nature* **2008**, *456*, 222–225.
- [22] D. A. Shapiro, Y.-S. Yu, T. Tyliczszak, J. Cabana, R. Celestre, W. Chao, K. Kaznatcheev, A. L. D. Kilcoyne, F. Maia, S. Marchesini, Y. S. Meng, T. Warwick, L. L. Yang, H. A. Padmore, *Nat. Photonics* **2014**, *8*, 765–769.
- [23] A. M. Wise, J. N. Weker, S. Kalirai, M. Farmand, D. A. Shapiro, F. Meirer, B. M. Weckhuysen, *ACS Catal.* **2016**, *6*, 2178–2181.
- [24] D. E. Perea, I. Arslan, J. Liu, Z. Ristanović, L. Kovarik, B. W. Arey, J. A. Lercher, S. R. Bare, B. M. Weckhuysen, *Nat. Commun.* **2015**, *6*, 7589.
- [25] S. Kalirai, P. P. Paalanan, J. Wang, F. Meirer, B. M. Weckhuysen, *Angew. Chem. Int. Ed.* **2016**, *55*, 11134–11138; *Angew. Chem.* **2016**, *128*, 11300–11304.
- [26] J. E. Schmidt, L. Peng, A. L. Paioni, H. L. Ehren, W. Guo, B. Mazumder, D. A. Matthijs de Winter, Ö. Attila, D. Fu, A. D. Chowdhury, K. Houben, M. Baldus, J. D. Poplawsky, B. M. Weckhuysen, *J. Am. Chem. Soc.* **2018**, *140*, 9154–9158.
- [27] A. Devaraj, M. Vijayakumar, J. Bao, M. F. Guo, M. A. Derewinski, Z. Xu, M. J. Gray, S. Proding, K. K. Ramasamy, *Sci. Rep.* **2016**, *6*, 37586.
- [28] J. E. Schmidt, J. D. Poplawsky, B. Mazumder, Ö. Attila, D. Fu, D. A. M. de Winter, F. Meirer, S. R. Bare, B. M. Weckhuysen, *Angew. Chem. Int. Ed.* **2016**, *55*, 11173–11177; *Angew. Chem.* **2016**, *128*, 11339–11343.
- [29] J. E. Schmidt, R. Oord, W. Guo, J. D. Poplawsky, B. M. Weckhuysen, *Nat. Commun.* **2017**, *8*, 1666.
- [30] L. Kovarik, N. M. Washton, R. Kukkadapu, A. Devaraj, A. Wang, Y. Wang, J. Szanyi, C. H. F. Peden, F. Gao, *ACS Catal.* **2017**, *7*, 2458–2470.
- [31] L. R. Aramburo, E. De Smit, B. Arstad, M. M. Van Schooneveld, L. Sommer, A. Juhin, T. Yokosawa, H. W. Zandbergen, U. Olsbye, F. M. F. De Groot, B. M. Weckhuysen, *Angew. Chem. Int. Ed.* **2012**, *51*, 3616–3619; *Angew. Chem.* **2012**, *124*, 3676–3679.
- [32] H. E. van der Bij, L. R. Aramburo, B. Arstad, J. J. Dynes, J. Wang, B. M. Weckhuysen, *ChemPhysChem* **2014**, *15*, 283–292.
- [33] H. E. van der Bij, F. Meirer, S. Kalirai, J. Wang, B. M. Weckhuysen, *Chem. Eur. J.* **2014**, *20*, 16922–16932.
- [34] L. R. Aramburo, J. Ruiz-Martinez, L. Sommer, B. Arstad, R. Buitrago-Sierra, A. Sepúlveda-Escribano, H. W. Zandbergen, U. Olsbye, F. M. F. de Groot, B. M. Weckhuysen, *ChemCatChem* **2013**, *5*, 1386–1394.
- [35] N. Jiang, *Reports Prog. Phys.* **2015**, *79*, 16501.
- [36] S. Calvin, *XAFS for Everyone*, CRC Press, Boca Raton, **2013**.
- [37] S. J. Schmiege, S. H. Oh, C. H. Kim, D. B. Brown, J. H. Lee, C. H. F. Peden, D. H. Kim, *Catal. Today* **2012**, *184*, 252–261.
- [38] J. H. Kwak, D. Tran, S. D. Burton, J. Szanyi, J. H. Lee, C. H. F. Peden, *J. Catal.* **2012**, *287*, 203–209.
- [39] A. Wang, Y. Wang, E. D. Walter, N. M. Washton, Y. Guo, G. Lu, C. F. Peden, F. Gao, *Catal. Today* **2019**, *320*, 91–99.
- [40] Y. Zhang, H. Wang, R. Chen, *RSC Adv.* **2015**, *5*, 67841–67848.
- [41] M. Guisnet, F. R. Ribeiro, *Deactivation and Regeneration of Zeolite Catalysts*, Imperial College Press, London, **2011**.
- [42] M. K. Miller, K. F. Russell, G. B. Thompson, *Ultramicroscopy* **2005**, *102*, 287–298.
- [43] M. K. Miller, K. F. Russell, *Ultramicroscopy* **2007**, *107*, 761–766.
- [44] K. Thompson, D. Lawrence, D. J. Larson, J. D. Olson, T. F. Kelly, B. Gorman, *Ultramicroscopy* **2007**, *107*, 131–139.
- [45] T. Warwick, K. Franck, J. B. Kortright, G. Meigs, M. Moronne, S. Myneni, E. Rotenberg, S. Seal, W. F. Steele, H. Ade, A. Garcia, S. Cerasari, J. Denlinger, S. Hayakawa, A. P. Hitchcock, T. Tyliczszak, J. Kikuma, E. G. Rightor, H. J. Shin, B. P. Tonner, *Rev. Sci. Instrum.* **1998**, *69*, 2964–2973.
- [46] E. G. Rightor, A. P. Hitchcock, H. Ade, R. D. Leapman, S. G. Urquhart, A. P. Smith, G. Mitchell, D. Fischer, H. J. Shin, T. Warwick, *J. Phys. Chem. B* **1997**, *101*, 1950–1960.
- [47] H. Bluhm, K. Andersson, T. Araki, K. Benzerara, G. E. Brown, J. J. Dynes, S. Ghosal, M. K. Gilles, H. C. Hansen, J. C. Hemminger, A. P. Hitchcock, G. Ketteler, A. L. D. Kilcoyne, E. Knedler, J. R. Lawrence, G. G. Leppard, J. Majzlam, B. S. Mun, S. C. B. Myneni, A. Nilsson, H. Ogasawara, D. F. Ogletree, K. Pecher, M. Salmeron, D. K. Shuh, B. Tonner, T. Tyliczszak, T. Warwick, T. H. Yoon, *J. Electron Spectrosc. Relat. Phenom.* **2006**, *150*, 86–104.
- [48] A. M. Beale, J. Ruiz-Martinez, B. M. Weckhuysen, in *In-Situ Charact. Heterog. Catal.*, John Wiley & Sons, Hoboken, **2013**, pp. 441–473.
- [49] Y. Liu, F. Meirer, P. A. Williams, J. Wang, J. C. Andrews, P. Pianetta, *J. Synchrotron Radiat.* **2012**, *19*, 281–287.
- [50] J. D. Poplawsky, J. E. Schmidt, B. Mazumder, W. Guo, Ö. Attila, D. Fu, D. A. M. de Winter, F. Meirer, S. R. Bare, B. M. Weckhuysen, *Microsc. Microanal.* **2017**, *23*, 674–675.

Manuscript received: August 25, 2018
Version of record online: ■ ■ ■